This is a repository copy of *Development of Ni-free Mn-stabilised maraging steels using Fe2SiTi precipitates*.

White Rose Research Online URL for this paper:
https://eprints.whiterose.ac.uk/146857/

Version: Accepted Version

Accepted Manuscript

Development of Ni-free Mn-stabilised maraging steels using Fe$_2$SiTi precipitates

Alexander.J. Knowles, Peng Gong, Khandaker.M. Rahman, W.Mark Rainforth, David Dye, Enrique.I. Galindo-Nava
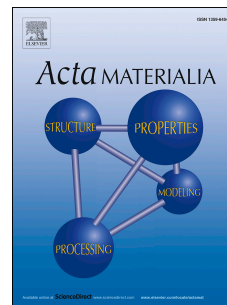
Please cite this article as: A.J Knowles, P. Gong, K.M Rahman, W.M. Rainforth, D. Dye, E.I Galindo-Nava, Development of Ni-free Mn-stabilised maraging steels using Fe$_2$SiTi precipitates, *Acta Materialia*, https://doi.org/10.1016/j.actamat.2019.05.034.
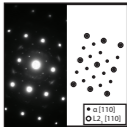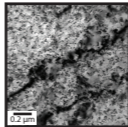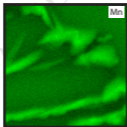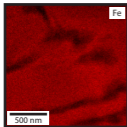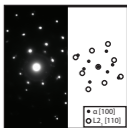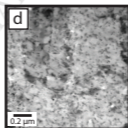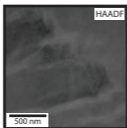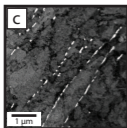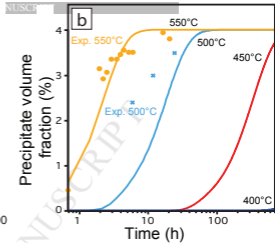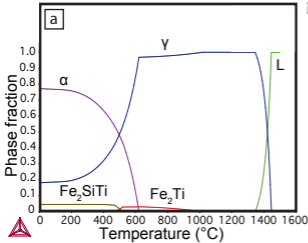
Fe-Mn-Si-Ti alloy a) CALPHAD design, b) Precipitation kinetics model, Characterisation of c) Mn stabilised austenite, d) Fe_2SiTi precipitates

Development of Ni-free Mn-stabilised maraging steels using Fe$_2$SiTi precipitates

Alexander J Knowles[a,b,*], Peng Gong[c], Khandaker M Rahman[a], W Mark Rainforth[c], David Dye[a], Enrique I Galindo-Nava[d]

[a]*Department of Materials, Imperial College, South Kensington, London SW7 2AZ, UK*
[b]*School of Metallurgy and Materials, University of Birmingham, Birmingham, B15 2TT, UK*
[c]*Department of Materials Science and Engineering, University of Sheffield, Sir Robert Hadfield Building, Mappin Street, Sheffield, S1 3JD*
[d]*Department of Materials Science and Metallurgy, University of Cambridge, Cambridge CB3 0F3, UK*

Abstract

Computational alloy design has been used to develop a new maraging steel system with low cost, using Mn for austenite reversion and Heusler Fe$_2$SiTi nm-scale precipitates to strengthen the martensite, avoiding high cost alloying elements such as Ni and Co. A pronounced ageing response was obtained, of over 100 HV, associated with the formation of 2-30nm Fe$_2$SiTi precipitates alongside the development of $\sim$10% Mn rich austenite, at the martensite boundaries with the Kurdjumov-Sachs orientation relationship. The precipitates took on different orientation relationships, depending on the size scale and ageing time, with fine $\sim$ 5 nm precipitates possessing an $<100>_{L2_1}//<100>_\alpha$ orientation relationship, compared to larger $\sim$ 20 nm precipitates with $<110>_{L2_1}//<100>_\alpha$. Computational alloy design has been used for the development and demonstration of an alloy design concept having multiple constraints. Whilst in this case computational design lacked the fidelity to completely replace experimental optimisation, it identifies the importance of embedding Thermodynamic and kinetic modelling within each experimental iteration, and vice versa, training the model between experimental iterations. In this approach, the model would guide targeted experiments, the experimental results would then be taken into future modelling to greatly accelerate the rate of alloy development.

Keywords: Steels, Precipitation, Microstructure, Mechanical Properties, Transmission Electron Microscopy

---

*Corresponding Author. a.j.knowles@bham.ac.uk

1. Introduction

Maraging steels comprising a martensitic matrix strengthened by intermetallic precipitates demonstrate exceptional combinations of high strength and toughness [1, 2]. However, their widespread use has been limited by their high cost (>£1,600-7,200 per tonne, Table 1). A large portion of this cost is due to alloying with the austenite stabilisers Ni and Co, which control the (lath) martensite start temperature (M_s) and promote the formation of reverted face-centred-cubic (fcc) austenite for improved ductility [3, 4]. The strength of these steels is based on the precipitation during ageing of nm-scale intermetallics, a variety of which are employed, such as $D0_{24}$ $Ni_3(Ti,Mo)$, ordered body-centred-cubic (bcc) intermetallic precipitates such as B2 NiAl and NiMn, or $L2_1$ Heusler structured intermetallics, e.g. Ni_2TiAl and Ni_2AlMn, as well as G phase $Ni_{16}Si_7Ti_6$ [5, 4, 6, 7]. Ordered bcc precipitates are of particular interest since they can be coherent with the martensitic ferrite matrix, providing hard particle strengthening as well as misfit strain strengthening of the surrounding matrix. These precipitates are typically non-shearable as their slip system $\langle 100 \rangle \{010\}$ does not allow for order hardening via e.g. pairs of bcc $\frac{1}{2}\langle 111 \rangle \{1\bar{1}0\}$-type dislocations [8].

However, the inclusion of Ni and other alloying additions for precipitate formation further increase the expense of such alloys. Past studies have highlighted the potential of the Heusler $L2_1$ Fe_2SiTi [9, 10] as an alternative strengthening phase that has greatly reduced elemental cost. Fe_2TiSi (a = 5.72 Å[11]) has a larger misfit (calculated as per [12]) of $\sim 2.5\%$ than NiAl (NiAl a = 2.89Å[13]) $\sim 1.6\%$, which could be anticipated to increase the misfit strain strengthening contribution. Recent lean maraging steels and advanced high strength steels (AHSS) with transformation induced plasticity (TRIP) have been successful in utilising Mn as the austenite stabiliser, greatly reducing Ni contents [14, 4].

Therefore it is interesting to ask whether it is possible to use Mn for austenite reversion to provide 100-200 nm reverted austenite films at martensite lath boundaries (for ductility), in combination with ~ 5 nm-scale $L2_1$ Fe_2SiTi precipitates aged into the martensite, and thereby produce a maraging steel with greatly reduced elemental cost. It is also interesting to ask whether computational alloy design is of sufficient maturity to guide such an alloy design effort, or whether brute-force experimental optimisation is still required.

[Table 1 about here.]

2. Computational alloy design

The systematic design approach proposed here uses appropriate composition–process–microstructure–property relationships. The first step was to model the phase equilibria using the Thermocalc TCFe8 database to examine an appropriate range of Fe-Mn-Si-Ti alloys that precipitate Fe_2SiTi and form austenite. The aim of the simulations was to determine the tradeoff between precipitation hardening and austenite reversion to maximise mechanical properties whilst

2

ensuring processability, *i.e.*, avoiding δ ferrite formation on solidification, possessing a single phase austenite region for hot working operations and forming only martensite on quenching. Figure 1a shows the predicted volume fraction of Fe_2SiTi when varying Si and Ti contents between 0.5-2 wt% and with a fixed Si/Ti ratio of 1; when Si=Ti=0.5 wt.% Fe_2SiTi is only stable up to about 425 °C, whereas if Si=Ti=1 wt.% Fe_2SiTi is stable up to 475 °C. A maximum volume fraction of 9 % is obtained when Si=Ti=2 wt.% and it remains approximately constant up to about 525 °C. The results suggest a possible ageing window between 450 and 525 °C and Si and Ti additions between 1 and 2 wt.%.

Previous work showed that grain–boundary embrittlement due to Mn segregation to the prior–austenite boundaries can in principle be avoided if the volume fraction of reverted austenite, f_γ, is high enough to allow Mn redistribution [4]. It was found that at least 25 % austenite is required in order to avoid grain–boundary embrittlement and the Mn content is tailored such that $f_\gamma \geq 30\%$ is formed at equilibrium at the ageing temperature. Figure 1 (b) shows the variation in the austenite fraction with temperature for Mn contents of 8–12 wt.% in Fe-xMn-1Si-1Ti (wt.%); calculations with different Si and Ti contents yielded similar results for f_γ. Adding at least 10 wt.% Mn ensures that $f_\gamma > 30\%$ in the ageing range 450–525 °C. Figures 1(c)–(d) show the predicted equilibrium phase diagrams for Fe-10Mn-1Si-1Ti and Fe-10Mn-2Si-2Ti, respectively. Figure 1(d) indicates that the composition Fe-10Mn-2Si-2Ti forms δ ferrite in upon solidification and is stable in the austenitic range. This may be problematic when hot rolling and prevent a complete transition to martensite upon quenching. Additional simulations changing the Mn content between 8 and 12 wt.%, with 2 wt.% of both Si and Ti, did not show improvements in removing the δ ferrite region. The alloy composition was therefore defined as Fe-10Mn-1Si-1Ti.

A final consideration to confirm the steel composition is that the fraction of retained austenite, $f_{retained}$, should be minimal. Retained austenite strongly affects the formation of reverted austenite and also has been reported to have detrimental effects on the yield strength [15]. It has been estimated that up to $\sim 5\%$ of $f_{retained}$ does not have significant influence in steel's mechanical properties [15]. The fraction of austenite is modelled using Koistinen and Marburger's equation [16]:

$$f_{\text{retained}} = \exp(-0.011(M_s - 25)) \tag{1}$$

where M_s is the martensite start temperature in °C. M_s is calculated using a recent model for martensite formation. A polynomial expression for M_s in terms of the steel's nominal composition was obtained; details of the model can be found in [17]. Table 1 shows the predicted M_s and $f_{retained}$ in the steels under comparison. The experimental M_s values for C300 and M350 are 190 °C [18] and 135 °C [19], respectively, showing that the model is in good agreement. The fraction of retained austenite predicted for Fe-10Mn-1Si-1Ti is within the range where no influence on the yield stress is expected and its M_s is similar to other conventional maraging steels, therefore a lath structure is anticipated.

The results obtained suggest that quenching and aging Fe-10Mn-1Si-1Ti at

3

450-500 °C is sufficient to develop both austenite and Fe$_2$SiTi phases and a very low fraction of retained austenite, although ageing at 500 °C is anticipated to yield relatively little precipitation hardening. Additional modelling of phase kinetics enables the prediction of the precipitate volume fraction and size, which 90 are utilised to predict the age hardening response and determine whether the reverted austenite forms at similar times than Fe$_2$SiTi.

[Figure 1 about here.]

2.1. Precipitation kinetics and hardness modelling

A modelling framework for prescribing the microstructure and strength in 95 maraging steels has been proposed in previous work with the emphasis on alloy optimisation [4]. The models were based on describing the hierarchical structure of the martensitic matrix, including the density of dislocations, laths, and high–angle grain boundaries. This microstructural model enabled the introduction of evolution equations for precipitation thermo-kinetics and lath–shaped austen-100 ite. Existing precipitation approaches for the average precipitate radius, r_p, and volume fraction, f_p, of Fe$_2$TiSi are adopted to predict the steel's age hardening response at 400 °C, 450 °C and 500 °C [20]. Details of the precipitation modelling are presented in the Appendix.

The strength of maraging steels stems primarily from three mechanisms [4]: 105 (1) the strength of lath martensite σ_{Mart}, (2) intermetallic precipitate hardening σ_p and (3) solid solution hardening σ_{ss}. In the absence of a better model, these are assumed to be additive:

$$H_v = \frac{1}{3}(\sigma_{\text{Mart}} + \sigma_p + \sigma_{ss}), \tag{2}$$

where the 1/3 factor accounts for the conversion between yield strength and hardness in steels. The strength of martensite is controlled by the increase in 110 grain boundary area and dislocation density:

$$\sigma_{Mart} = \frac{k_{HP}}{\sqrt{d_{block}}} + 0.25M\mu b\sqrt{\rho}, \tag{3}$$

where the block size, d_{block}, is considered the effective grain size, $k_{HP} = 300$ MPa μm$^{1/2}$, $M = 3$ is the Taylor average orientation factor, μ is the shear modulus, b the dislocation Burgers vector and ρ the dislocation density. d_{block} was obtained in previous work, showing that it is proportional to the prior 115 austenite grain size D_g [4]: $d_{block} = 0.067D_g$. Since the initial austenite grain size was not defined as a design parameter, a block size of $d_{block} = 7$ μm was adopted, as this value has been found to be the maximum block size reported in several martensitic steels [21]. The dislocation density in maraging steels is given by [17]:

$$\rho = \frac{3E}{(1+2\nu^2)\mu} \frac{4\varepsilon^2 w_{lath}}{d_{lath}^2 b} \tag{4}$$

4

where d_{lath} is the lath size (approximately constant $d_{lath} = 250$ nm), $E = 80$ GPa is the Young's modulus, $w_{lath} = 4$ nm is the width of a lath boundary and $\varepsilon = 0.24$ is the (Bain) transformation strain between fcc and bcc.

The precipitation strengthening term is given by the Orowan equation, as it is assumed that the intermetallics are not shearable:

$$\sigma_p = 0.1\mu b \frac{\sqrt{f_p}}{r_p} \ln\left(\frac{r_p}{b}\right). \tag{5}$$

where r_p and f_p are the average precipitate radius and volume fraction. The solid solution strengthening term, σ_{ss} is calculated using Labusch's classical model for point–like defects pinning dislocations, which we have previously been examined for Mn, Ti and Si-containing maraging steels [4].

The model predictions for Fe_2SiTi when ageing the maraging steels at 400 and 450 °C are shown in Figure 2; no ageing response was produced at 500 °C and this result was omitted. Additionally, experimental results (dots) for Fe-1Ti-2.5Si (wt%) reported in [9] are used to test the fidelity of the model; in this case the ageing results are for 500 and 550 °C. The interfacial energy was fixed equal to 90 mJ m^{-2} in both cases. Figures 2(a) and (b) show the volume fraction and average radius variation of Fe_2SiTi. The predicted volume fraction at 500 and 550 °C is consistent with the values measured by Perrier et al. [9], however the experimental radii are smaller in both conditions. A possible reason for the discrepancies is that these authors have argued that two species of Fe_2SiTi intermetallics form during ageing [22, 23], the primary precipitates form at early stages of ageing but remain very fine ($r_p \leq 5$ nm) and could not be resolved in their TEM work, whereas the secondary particles coarsen at levels where they could be resolved by TEM (radius $\sim$10 nm). They have confirmed the presence of small scale precipitates using atom probe tomography, but the phase chemistry differed slightly from the equilibrium composition of Fe_2SiTi; this is probably due to the higher Si content in their Fe-1Ti-2.5Si alloy. These effects have not been included in the model and a unimodal particle size distribution is assumed. In addition, based in their results [22, 23, 9], it is apparent that the higher Si content increases the solution temperature of Fe_2SiTi; however, additional Thermocalc simulations for Fe-10Mn-1Ti-1.5Si predicted δ ferrite forming at higher temperatures (similar to Figure 1(d)). Therefore, the higher Si additions not being suitable for steel processing.

The predicted hardness values using the precipitate radius and volume fraction data from Figure 2(a) and (b), including Fe-10Mn-1Ti-1Si and Fe-1Ti-2.5Si, are shown in Figure 2(c). It is worth noting that for the case of Fe-1Ti-2.5Si at 500 and 550 °C, the matrix is ferritic and the initial hardness is lower, $\sim$ 180 HV; for these conditions the model is able to describe the hardening rate arising from Fe_2SiTi but the net increase in hardness is less significant; the discrepancy again can be related to the possible presence of fine scale precipitates not accounted for in the model. As for the Fe-10Mn-1Si-1Ti case (400 and 450 °C), the predictions are useful to identify and ageing window for the peak hardness 450 °C to be 200-400 h, whereas more than 200 hours are necessary to produce any notice-

5

able hardening when ageing at $400\,^{\circ}$C. In the former condition, the hardness is estimated to increase up to 85 HV by precipitation strengthening.

[Figure 2 about here.]

165 *2.2. Austenite reversion*

The evolution of reverted austenite in maraging steels is affected by the pre-existing α' laths, as the austenite nucleates at the lath boundaries and it is restricted to grow along the lath boundaries. A model for describing the volume fraction of reverted austenite f_γ in terms of the average austenite thickness, r_γ, **170** and length, L_γ, has been introduced in previous work [4]:

$$f_\gamma = \frac{r_\gamma^2 L_\gamma}{d_{lath}^2 d_{block}}. \tag{6}$$

Details of the evolution equations for r_γ and L_γ are shown in the Appendix.

Figure 2(d) shows the predicted austenite fraction when ageing at 450, 500 and $550\,^{\circ}$C. A very small fraction of austenite forms after 1000 h of ageing at $450\,^{\circ}$C (7 %), whereas 30% of austenite forms after 1000 hours of ageing at **175** $500\,^{\circ}$C and after 75 hours of ageing at $550\,^{\circ}$C; however there is no hardening response from Fe$_2$SiTi at 500 and $550\,^{\circ}$C. The austenite fraction in the optimal range for peak hardness ($450\,^{\circ}$C and ~ 200 hours) is predicted to be 2%, which lies below the levels necessary to avoid grain boundary embrittlement [4].

The model predictions indicate that the best tradeoff in properties in Fe-**180** 10Mn-1Si-1Ti occur when ageing at $450\,^{\circ}$C but it is not enough to form at least 25% of reverted austenite. The simulations also confirm that tailoring significant intermetallic strengthening whilst promoting the formation of the tough reverted austenite is still a challenge for C–free maraging steels.

3. Experimental Methods

185 A single 400g ingot was prepared by arc melting of pure ($> 99.9\%$) elements under Ar, with the composition of Fe-10Mn-1Si-1Ti (wt.%) instructed by computational alloy design. LECO combustion analysis of the as-cast alloy determined a carbon content of 89 wppm and nitrogen content of 42 wppm. Additional Thermocalc calculations of the designed steel with these C and N **190** levels were performed. The small additions of C and N yield only to 0.11 % of Ti(CN) across the temperatures tested, confirming that most Ti is available for the Heusler precipitates; the predicted composition of the carbon-nitride is 53.4Ti-33.2C-13.4N wt%. As for the other phases, Thermocalc simulations showed that the nature of the designed phases, their volume fraction and sta-**195** bility were largely unchanged. As for the variation in the M_s temperature, the predicted values for the steel with C and N was $267\,^{\circ}$C, only $6\,^{\circ}$C lower than the C and N–free designed steel (Table 1), whereas the predicted retained austenite is 7%, only 0.5% higher than for the C and N–free version. This also confirms that small amounts of C and N will not modify the formation of martensite. As

6

for phase kinetics, the interfacial energy is the only parameter that can possibly be affected by changes in steel composition but since C and N form precipitate phases across the temperatures tested, the composition and structure of the matrix, Heusler precipitates and austenite were unchanged and it can be assumed that the energy will remain unaltered by C and N additions. Sections of the ingot were encapsulated within evacuated glass ampoules backfilled with argon and were homogenised at $1200\,°C$ for 24 hours and water quenched. The sections were then hot flat rolled from 12 mm down to 3 mm in three passes at 35% strain per pass at $1200\,°C$. Following rolling the alloy was recrystallised at $1200\,°C$ for 15 min and water quenched; minimal changes in hardness were found between rolling and recrystallisation treatments at 1000, 1100 and $1200\,°C$ for times of 5, 10 and 15 min. Sections from the recrystallised alloy, encapsulated within evacuated glass ampoules backfilled with argon, were aged at 400, 450, 500 or $550\,°C$ for 1 h to 4 weeks, followed by air cooling. Hardness indents using a 1 kg load held for 10 s were made, averaging five measurements.

Scanning electron microcopy (SEM) was performed on a Zeiss Sigma and a JEOL 5800 operated at 5 or 10 kV for imaging and at 20 kV for energy-dispersive X-ray spectrometry (EDX). A 20 kV acceleration voltage and emission current of $200\,\mu A$ were used at a specimen tilt of $70°$ and a step size of $0.1 - 0.3\,\mu m$. Electron backscatter diffraction (EBSD) was performed on an FEI Nova NanoSEM 450 microscope using an Oxford Instruments EBSD camera and analysed with HKL Channel 5 software.

Transmission electron microscopy (TEM) and scanning TEM (STEM) were performed using JEOL 2100F, JEOL 2010F and Philips 420 microscopes. TEM foils were prepared by focussed ion beam (FIB) lift outs or by mechanical thinning 3 mm discs to $150\,\mu m$ followed by eletropolishing using a Fischione twin-jet electropolishing unit, with a solution of 5% perchloric acid, 60% methanol and 35% butyl alcohol at a temperature of $-40\,°C$. FIB lift-outs were prepared using an FEI-Helios dual-beam FIB with phases identified from etched optical micrographs, with a protective Pt deposited on the surface prior to trenching, thinning, lift-out and final thinning. Further TEM samples were prepared by the carbon replica method.

4. Results

[Figure 3 about here.]

Ageing heat treatments were applied to the alloy in order to promote the formation of reverted austenite as well as Fe_2SiTi at 400, 450, 500 or $550\,°C$. No ageing response was found at temperatures of $550\,°C$ for 20 h or $500\,°C$ for 20 and 200 h. Ageing responses were determined at 400 and $450\,°C$ from which ageing curves from 1 h to 4 weeks were produced, Figure 3. $400\,°C$ heat treatment resulted in a higher hardness at each time. However, peak hardness was still not reached even after 4 weeks of ageing, where an increase in hardness of 110 HV. In contrast, at $450\,°C$ a peak hardness of 348 HV was reached after 8 days (192 hours) representing an increase in hardness of nearly 80 HV, which

7

is in agreement with the model prediction (Figure 2). The pronounced increase in hardness at 400 and 450 °C indicated that precipitation of a hard phase or phases had occurred, anticipated to be L2$_1$ Heusler Fe$_2$SiTi intermetallic phase.

[Figure 4 about here.]

In order to understand the microstructural changes resulting in the age hardening of the alloys microscopy was performed, Figure 4. In the recrystallised condition a martensitic lath microstructure was observed, Figure 4a, which was maintained following ageing, Figure 4b-c. Ageing of the alloy resulted in a second phase being observed after 8 days and 4 weeks, Figure 4c and d. The second phase was darker than the matrix phase when imaged using a backscattered electron (BSE) detector, indicating lower average atomic number (Z). The volume fraction of second phase was found to increase on increased ageing time.

The X-ray diffraction (XRD) pattern collected from the alloy in the 4 week condition shown in Figure 4g found strong ferrite reflections as well as austenite reflections suggesting that the second phase observed by SEM (Figure 4c and d) was austenite, which was consistent with the Z contrast observed given the higher Mn content predicted in austenite. No clear L2$_1$ reflections indicative of the Fe$_2$SiTi were observed. However, many of these would overlap with the ferrite reflections, while the superlattice reflections were predicted to be weak and so at the ~ 4 vol.% quantities calculated may not be visible.

[Figure 5 about here.]

Figure 5 presents inverse pole figure (IPF), martensite grain distribution, phase distribution and band contrast maps of the alloy aged at 450 °C for 4 weeks obtained by EBSD. In the IPF-Z map (Figure 5a) recrystallised equiaxed prior austenite grains could be observed as well as lath martensite grains. The prior austenite grain size was determined to be $\sim 95\,\mu$m by the linear intercept method. The grain boundary map (Figure 5b) highlights that high angle grain boundaries with misorientations larger than $15\,^\circ$ predominated between the lath martensite grains, whilst within laths subgrain boundaries misorientated $< 15\,^\circ$ were observed. The driving pressure for the growth of such recrystallisation grains is the stored energy associated with the dislocations introduced during prior straining. The EBSD analysis found that the nano-sized phase present at lath boundaries in Figure 4 corresponded to fcc austenite as visualised in the phase distribution map (Figure 5c). This confirmed that the austenite reflections found by XRD (Figure 4g) correspond to the darker second phase in the BSE SEM micrographs (Figure 4e and f). Although CALPHAD may predict 20% Austenite at room temperature (Figure 1), this is kinetically restricted due to lack of diffusion and the high driving force of the martensitic transformation upon quenching, as accounted for in the models and validated by experiment. Martensite may form upon quenching from single-phase austenite (after annealing between 1000°C–1200°C). In the work of Martínez, *et al.* [24] it was shown that $\sim 97\,\%\ \alpha'$ forms upon quenching in Fe-10Mn, in spite of Thermocalc equilibrium predictions showing $\approx 17\,\%$ of austenite at room temperature. This

8

is because of the high driving force ($\approx$ 1255 J/mol [17]) for the martensitic transformation due to the large undercooling upon quenching. Our designed steel follows similar trends, with the high Mn content being the primary contributor to the martensite transformation kinetics. Owing to the austenite fraction being below the 25% target, the alloy's ductility was limited precluding tensile testing. However, much could be learnt from the microstructure of the unique triplex alloys, comprising: ferrite, Mn stabilised reverted austenite and Fe_2SiTi precipitates, prior to iterating the composition to target a higher austenite content.

[Figure 6 about here.]

TEM was employed to further study the phases present in an electropolished foil of the alloy aged at 450 °C for 8 days and in particular the second phase austenite at the martensite lath boundaries. The selected area diffraction pattern (SADP) shown in Figure 6a and b taken with a 200 nm aperture contained both ferrite and austenite reflections. From this it was determined that the Kurdjumov-Sachs (K-S) orientation relationship (OR) existed between ferrite and austenite of $(111)_\gamma//(110)_\alpha$, $<1\bar{1}0>_\gamma//<1\bar{1}1>_\alpha$ [25, 26] This was validated by tilting to other zone axes where the K-S OR was also found to be obeyed. STEM of a FIB lift-out foil of the alloy aged at 450 °C for 8 days is shown in Figure 6d-h. STEM-EDX clearly identified the anticipated segregation of Mn to the austenite phase identified at the martensite lath boundaries (Figure 6f). It was noted that the regions rich in Mn were also depleted in Si and Ti, suggesting that Si and Ti preferentially segregate to ferrite over austenite. It was also found that correlated regions of increased Si and Ti occurred at the austenite-ferrite boundaries as well as within the ferrite. These were suspected to be related to the Fe_2SiTi intermetallic phase.

[Figure 7 about here.]

TEM study of the martensite laths found small particles within the ferritic matrix, Figure 7. SADP analysis found that alongside ferrite reflections, reflections were also present consistent with the $L2_1$ Heusler Fe_2SiTi intermetallic phase with a lattice parameter of $\sim$5.7 Å. These were found to adopt the known $<100>_{L2_1}//<100>_\alpha$ orientation relationship. Additional reflections were also found, consistent with a $<110>_{L2_1}//<100>_\alpha$ orientation relationship. This indicated that two orientations of $L2_1$ precipitates existed in the aged alloy.

[Figure 8 about here.]

The carbon replica technique was used to prepare films containing precipitates from the alloy aged for 450 °C for 8 days and 450 °C for 4 weeks. In both conditions the ferrite was completely removed leaving solely the $L2_1$ Heusler Fe_2SiTi intermetallic precipitates, Figure 8a and b. It was found that the ageing time resulted in an increase in the size of the precipitates. In the 4 week

9

condition a bimodal distribution of precipitate size was found, indicative of two populations of the Heusler Fe_2SiTi precipitates, which was also noted visually within the 8 day condition.

₃₃₀ [Figure 9 about here.]

It was suspected that the bimodal size distribution observed in the carbon replica samples may be related to the two orientation relationships observed for $L2_1$ Fe_2SiTi precipitates in Figure 7. A SADP with $B \sim <110>$ identified both ORs described in Figure 7, as shown in Figure 9a. Dark field imaging from a ₃₃₅ {110} reflection (red) identified larger particles $\sim$15 nm in size, whilst imaging from {002} (green) for the other OR highlighted smaller particles $\sim$5 nm in size. To explore this further, HR-TEM was employed on an electropolished sample of the alloy aged at 450 °C for 8 days. The foil was tilted to a $[100]_\alpha$ zone axis where both sizes of precipitate could be observed. Taking a fast Fourier ₃₄₀ transform (FFT) of each region revealed the regions comprised a [110] zone axis in the larger precipitates (Figure 9e), in contrast to a [100] zone axis in the smaller precipitates (Figure 9f), matching that of the surrounding matrix.

5. Discussion

Due to the competition between precipitate and austenite development, a ₃₄₅ number of uncertainties existed as to whether higher aging temperatures may produce Fe_2SiTi. Fe_2SiTi is modelled within the TCFE8 database, but the accuracy of its stable temperature range must be considered. Fe_2SiTi has been reported as metastable [27], and, as with other phases, variations between predicted and experimental formation temperatures of $>$50 °C often reported, par- ₃₅₀ ticularly for less studied systems and those away from the optimised compositions of the database, e.g. the effect of dissolved Mn on Fe_2SiTi formation. It was also considered that the driving force to produce C14 Fe_2Ti from 500-1000°C (Figure 1c) may promote metastable $L2_1$ Fe_2SiTi. Fe_2SiTi, which could be anticipated to preferentially nucleate due to its coherent interfaces with lower ₃₅₅ surface energy and so smaller nucleation barrier. This is in analogy to Co-Al-W alloys where $L1_2$-γ' in easier to nucleate than B2 or $D0_19$ [?], owing to coherency strain and elastic contributions to the Gibbs free energy [?]. However, the predictions for Fe_2SiTi were in fact in good agreement with the experimental results, with the solvus found to be between $450 - 500$ °C. No C14 Fe_2Ti ₃₆₀ was observed at any temperature, which may have been kinetically inhibited.

Aging at 450 and 400 °C resulted in peak hardening of $\sim$ 80 HV in good agreement with the kinetic model developed for Ni containing steels, Figure 2. However, due to low aging temperatures, long times were needed, with a corresponding low austenite fraction. TEM and STEM analysis demonstrated that ₃₆₅ ageing produced spherical nanoscale $L2_1$ Fe_2SiTi. Bcc A2 and $L2_1$ SADPs were recorded (Figure 7) inconsistent with other possible phases, e.g. Fe_2Ti, or the FeSiTi τ_2 [27]. The $L2_1$ precipitates bore resemblance in form and size to $L2_1$ Ni_2AlTi precipitates within Ni maraging steels [28, 2]. However, a key difference

found for the Fe_2SiTi precipitates was that they formed with a bimodal popula-
tion. This was indicated qualitative by the additional frequency of 2-5 nm diam-
eter particles observed from the carbon replica method, Figure 8c. The bimodal
population was confirmed by dark field imaging where smaller precipitates were
found to adopt a cube-cube $<100>_{L2_1}//<100>_\alpha$ orientation relationship, as is
the case for B2 NiAl and $L2_1$ Ni_2AlTi. Whereas, larger Fe_2SiTi precipitates had
a $<110>_{L2_1}//<100>_\alpha$ orientation relationship. Additional work is needed to
determine their formation mechanism, as there are no reports of such behaviour
in Fe-Mn-Si-Ti.

From a modelling standpoint, using a smaller interfacial energy of $\gamma_{int} = 20$
mJ m^{-2}, compared to $\gamma_{int} = 90$ mJ m^{-2} for the results in Figure 2, is sufficient
to predict the size of the smaller precipitates forming in Fe-1Ti-2.5Si at 500 °C
and 550 °C. A possible explanation for bimodal distributions forming in these
steels can be attributed to small fluctuations in the local composition, as local
composition variations are primarily responsible for controlling the precipitate
interfacial energy [29]. In addition, the fact that their orientation relationships
are different also suggests that variations in the local lattice misfit can influence
the growth and coarsening of these precipitates.

5.1. Competition between austenite formation and intermetallic precipitation

The slower precipitation kinetics make Fe_2SiTi attractive over NiAl, Ni_3Ti or
Cu (in bcc clusters) as it could enable Mn–stabilised austenite and precipitates
to be developed simultaneously. While for Ni or Cu precipitates their fast
coarsening making it challenging to develop sufficient quantities of austenite
alongside peak precipitation hardening. To explore this, simulations of steels
containing 10% Mn and different alloying additions (Table 2) to induce $\sim 4\%$ of
precipitates were made and the time to reach peak hardness with temperature
calculated, Figure 10 (details in Appendix). For Ni_3Ti, Mn additions cannot
be made as it destabilises the intermetallic, instead calculations were performed
for larger 17.5 wt% additions of Ni required to induce comparable austenite
alongside Ni_3Ti.

[Figure 10 about here.]

[Table 2 about here.]

The 10% Mn reverted austenite formation calculations (Figure 9 blue curve)
found that at 575 °C it took 10 hours for 30% reversion, whereas 500 °C required
over 2000 hours. As expected, simulations at 500 °C found Fe_2SiTi (red curve)
to form much earlier than austenite in spite of its slower kinetics than the
other intermetallics. Extrapolation of Fe_2SiTi stability to higher temperatures
(dotted orange line), indicated that, in principle, its kinetics would mach those
for the austenite, and thereby match peak hardness and austenite fraction at
relatively short ageing times. Whilst this was not possible in the Fe-10Mn-1Si-
1Ti alloy, increasing the Si content to 2.5 wt% increases the Fe_2SiTi formation
temperature to 575 °C. However, this may be at the expense of formation of δ
ferrite above 1000 °C (Figure 1(a)), as previously discussed.

11

In contrast to Fe_2SiTi, the peak hardness for NiAl (Figure 9 purple curve) at 500 °C was reached after only 2 h, whereas much longer time is required for austenite reversion. Similarly, the peak hardness for Ni_3Ti (light blue) also
415 happens faster than austenite formation. For Cu precipitates (green curve), high temperatures >575 °C can in principle form simultaneously with the desired austenite content. However, in practice, their formation at higher temperatures can be compromised, as the metastable bcc clusters transition to the equilibrium face–centred cubic phase [30]. It is worth highlighting that the difference in the
420 kinetics of precipitation are strongly influenced by the effective diffusivity of their forming elements in Fe. With the model able to work across a range of systems, Ni containing [4] and Ni–free maraging steels, the present analysis is valuable in defining accelerated paths to new alloys, where a single targeted alloy composition can be evaluated, rather than defining a time–consuming matrix of
425 multiple compositions.

Whilst the present Fe-Mn-Si-Ti alloy did not simultaneously achieve the targeted intermetallic precipitation alongside $f_\gamma \sim 25\%$ austenite revision. It demonstrated that the Ni-free system can achieve the desired three-phases of martensitic ferrite, reverted austenite and intermetallic precipitation. This
430 new Ni-free alloy concept utilising Mn for austenite reversion and Fe_2SiTi for strengthening offers new prospects for radically cheaper maraging steels, however, further iteration is needed, both experimentally and for the predictive models.

The onward development of Fe-Mn-Si-Ti based steels must address the limited
435 austenite fraction in order to improve their ductility. The first means to address this is to increase the Si and Ti content to increase the Fe_2SiTi solvus temperature (Figure 1d) and so enable a higher ageing temperature with accelerated austenite reversion (Figure 10). However, as discussed, this risks the formation of delta ferrite (Figure 1d). A second approach, would be to increase the
440 Mn content or even to include modest Ni additions to help promote austenite formation over delta. With the alloy not containing Al, Ni may segregate principally to austenite, rather than the precipitates, reducing the alloying additions needed compared to traditional maraging steels. However, study is needed as to the balance of phases formed against their relative variations in composition.
445 Although our computational alloy design strategy worked to some extent, it did not capture several constraints faced in practice, such as the compromise between the dissimilar ageing times for fine-scale precipitation and sufficient austenite reversion (Fig. 10). A way to improve our design strategy can be to use computational methods incorporating multi-objective optimisation of alloys,
450 such as the one introduced in [31]. This approach would allow us to simultaneously explore wide range of combinations in alloy composition and processing parameters that can tackle the constraints faced in this work; this could be done combining genetic algorithms with Thermodynamic predictions for phase constituency and stability, the phase kinetic models for processability and possible
455 non-linear regression models for physical mechanisms not described by the models such as precipitates with bimodal populations. This can be done in future work.

12

6. Conclusions

- **A new maraging steel** based on the Fe-Mn-Si-Ti system has demonstrated it is possible to use Mn to stabilise austenite reversion and Heusler Fe_2SiTi nm-scale precipitates to strengthen the martensite. This offers the prospect of Ni and Co free high strength maraging steels with greatly reduced cost.

- **Mn stabilised reverted austenite**, formed at lath boundaries, was found to have behaviour to that stabilised by Ni. STEM-EDX was used to confirmed the segregation of Mn, whilst EBSD and TEM SAPDs confirmed its structure, and determined that the Kurdjumov-Sachs orientation was obeyed with the surrounding ferritic martensite.

- **Heusler L2$_1$ Fe$_2$SiTi precipitates**, were found to form within the martensitic laths on aging at $400\,^{\circ}$C and $450\,^{\circ}$C, with peak age hardening responses of 110 and 80 HV respectively. TEM revealed these precipitates to have a bimodal size distribution with the smaller $\sim 5\,$nm precipitates possessing an $<100>_{L2_1}//<100>_{\alpha}$ orientation relationship, whilst the larger $\sim 20\,$nm precipitates had a $<110>_{L2_1}//<100>_{\alpha}$ orientation relationship.

- **Model teaches experiment**: It was anticipated by the phase kinetics predictions that the optimal strength-elongation relationship in maraging steels, via simultaneous age hardening and reverted austenite formation, was going to be difficult. The predicted austenite structure was well in agreement against the measured fraction and thickness observed experimentally, indicating that higher temperatures are required to improve the ductility of the design steel.

- **Experiment teaches model**: A single population of precipitates was predicted. However, experimentally it was found that two distinct species of precipitates occurred, but the origins of such behaviour are not fully understood yet. An extension from the work here would be to iterate the model by including the dual population of precipitates, rationalising the formation mechanisms with additional analysis. This implementation would then allow us to move the model forward to better design the next generation of Fe-Mn-Si-Ti steels.

- **A combined approach** is needed to tackle the challenge of finding a composition and heat treatment where a maraging steel has 25%–30% reverted austenite, for good ductility, and fine–scale intermetallics, for high strength. By integrating computational alloy design with targeted experimentation the number of iterations to produce new alloys can be reduced and the development new alloys accelerated.

[1] H. Leitner, M. Schober, R. Schnitzer, S. Zinner, Strengthening behavior of Fe–Cr–Ni–Al–(Ti) maraging steels, Proceedings of the Second International ASM Conference on High Temperature Aluminides and Intermetalics: Part 2 528 (15) (2011) 5264–5270.

[2] L. Sun, T. H. Simm, T. L. Martin, S. McAdam, D. R. Galvin, K. M. Perkins, P. A. J. Bagot, M. P. Moody, S. W. Ooi, P. Hill, M. J. Rawson, H. K. D. H. Bhadeshia, A novel ultra-high strength maraging steel with balanced ductility and creep resistance achieved by nanoscale β-NiAl and Laves phase precipitates, Acta Materialia 149 (2018) 285–301.

[3] A. Markfield, A. Rosen, The Effect of Reverted Austenite on the Plastic-Deformation of Maraging-Steel, Materials Science and Engineering 46 (2) (1980) 151–157.

[4] E. I. Galindo-Nava, W. M. Rainforth, P. E. J. Rivera-Diaz-del Castillo, Predicting microstructure and strength of maraging steels: Elemental optimisation, Acta Materialia 117 (2016) 270–285.

[5] R. Schnitzer, R. Radis, M. N. hrer, M. Schober, R. Hochfellner, S. Zinner, E. Povoden-Karadeniz, E. Kozeschnik, H. Leitner, Reverted austenite in ph 13-8 Mo maraging steels, Materials Chemistry and Physics 122 (1) (2010) 138–145.

[6] J. Millán, S. Sandlöbes, A. Al-Zubi, T. Hickel, P. Choi, J. Neugebauer, D. Ponge, D. Raabe, Designing Heusler nanoprecipitates by elastic misfit stabilization in Fe–Mn maraging steels, Acta Materialia 76 (2014) 94–105.

[7] W. W. Sun, R. K. W. Marceau, M. J. Styles, D. Barbier, C. R. Hutchinson, G phase precipitation and strengthening in ultra-high strength ferritic steels: Towards lean 'maraging' metallurgy, Acta Materialia 130 (2017) 28–46.

[8] D. B. Miracle, S. Russell, C. C. Law, Slip system modification in NiAl, MRS Proceedings 133 (1989) 225–230.

[9] M. Perrier, A. Deschamps, O. Bouaziz, Y. Brechet, F. Danoix, F. De Geuser, P. Donnadieu, K. Hoummada, P. Maugis, Characterization and modeling of precipitation kinetics in a Fe-Si-Ti alloy, Metallurgical and Materials Transactions A: Physical Metallurgy and Materials Science 43 (13) (2012) 4999–5008.

[10] D. H. Jack, R. W. K. Honeycombe, Age hardening of an Fe-Ti-Si alloy, Acta Metallurgica 20 (1972) 787–796.

[11] M. Meinert, M. P. Geisler, J. Schmalhorst, U. Heinzmann, E. Arenholz, W. Hetaba, M. Stöger-Pollach, A. Hütten, G. Reiss, Experimental realization of a semiconducting full-Heusler compound: Fe2TiSi, Physical Review B 90 (8) (2014) 219.

[12] G. Ghosh, G. B. Olson, Integrated design of Nb-based superalloys: Ab initio calculations, computational thermodynamics and kinetics, and experimental results, Acta Materialia 55 (10) (2007) 3281–3303.

[13] N. Belyavina, V. Markiv, O. Nakonechna, F. Lozovyi, Phase equilibria in the Ni–Al–Ga system at 700 °c, Journal of alloys and compounds 593 (C) (2014) 41–49.

[14] P. Gong, E. J. Palmiere, W. M. Rainforth, Dissolution and precipitation behaviour in steels microalloyed with niobium during thermomechanical processing, Acta Materialia 97 (C) (2015) 392–403.

14

[15] M. El-Fawkhry, M. Eissa, A. Fathy, T. Mattar, Development of maraging steel with retained austenite in martensite matrix, Materials Today: Proceedings 2 (2015) S711 – S714.

[16] S. H. Chong, A. Sayles, R. Keyse, J. D. Atkinson, E. A. Wilson, Examination of microstructures and microanalysis of an Fe-9% Ni alloy, Materials Transactions, JIM 39 (1) (1998) 179–188.

[17] E. Galindo-Nava, On the prediction of martensite formation in metals, Scripta Materialia 138 (2017) 6 – 11.

[18] F. Zhu, Y. F. Yin, R. G. Faulkner, Microstructural control of maraging steel c300, Materials Science and Technology 27 (1) (2011) 395–405.

[19] Y. He, K. Yang, W. Sha, Microstructure and mechanical properties of a 2000 MPa grade Co-free maraging steel, Metall Mater Trans A 36 (2005) 2273–2287.

[20] J. Robson, Modelling the overlap of nucleation, growth and coarsening during precipitation, Acta Materialia 52 (15) (2004) 4669 – 4676.

[21] E. Galindo-Nava, P. Rivera-Díaz-Del-Castillo, A model for the microstructure behaviour and strength evolution in lath martensite, Acta Materialia 98 (2015) 81–93.

[22] M. Perrier, O. Bouaziz, Y. Brechet, A. Deschamps, P. Donnadieu, Mechanical properties of low carbon steel hardened by the Fe_2SiTi phase at high volume fraction, Journal of Physics: Conference Series 240 (2010) 012095.

[23] M. Perrier, A. Deschamps, P. Donnadieu, F. De Geuser, F. Danoix, O. Bouaziz, Y. Brechet, Precipitation sequence and kinetics in an Fe-Si-Ti alloy, Solid State Phenomena 172-174 (2011) 883–838.

[24] J. Martinez, S. Cotes, A. Cabrera, J. Desimoni, A. Fernandez Guillermet, On the relative fraction of η martensite in γ-Fe-Mn alloys, Mater Sci and Eng A 408 (2005) 26–32.

[25] U. Dahmen, Orientation relationships in precipitation systems, Acta Metallurgica 30 (2002) 63–73.

[26] X. D. LI, Z. D. YIN, Reverted austenite during aging in 18Ni(350) maraging-steel, Materials Letters 24 (4) (1995) 239–242.

[27] V. Raghavan, Fe-Si-Ti (Iron-Silicon-Titanium), Journal of Phase Equilibria & Diffusion 30 (4).

[28] F. Qian, J. Sharp, W. M. Rainforth, Characterisation of L21-ordered Ni2TiAl precipitates in FeMn maraging steels, Materials characterization 118 (C) (2016) 199–205.

[29] E. Kozeschnik, Modeling solid-state precipitation, Momentum press, 2013.

[30] G. Stechauner, E. Kozeschnik, Thermo-kinetic modeling of Cu precipitation in α-Fe, Acta Materialia 100 (2015) 135 – 146.

[31] E. Menou, G. Ramstein, E. Bertrand, F. Tancret, Multi-objective constrained design of nickel-base superalloys using data mining- and thermodynamics-driven genetic algorithms, Modelling Simul Mater Sci Eng 24 (2016) 1–25.

[32] M. Perez, D. Dumont, D. Acevedo-Reyes, Implementation of classical nucleation and growth theories for precipitation, Acta Mater 56 (2008) 2119–2132.

[33] London-Metal-Exchange, www.lme.com/metals.

[34] Metal-Bulletin, www.metalbulletin.com.

[35] ANTAM, www.antam.com.

[36] Infomine, www.infomine.com/investment/metal-prices.

[37] M. Hättestrand, J. Nilsson, K. Stiller, P. Liu, M. Andersson, Precipitation hardening in a 12%Cr-9%Ni-4%Mo-2%Cu stainless steel, Acta Mater 52 (2004) 1023–1037.

[38] R. Bhambroo, S. Roychowdhury, V. Kain, V. Raja, Effect of reverted austenite on mechanical properties of precipitation hardenable 17-4 stainless steel, Mater Sci Eng A 568 (2013) 127–133.

Appendix

A.1: Precipitation kinetics modelling

In order to simplify the analysis, modelling of single–component precipitation is assumed but an average diffusion coefficient between Ti and Si is considered: $D = \frac{2}{\frac{1}{D_{Ti}} + \frac{1}{D_{Si}}}$, where D_{Ti} and D_{Si} are the diffusion coefficients of Ti and Si in Fe, respectively; diffusion prefactors and activation energies for D_{Ti} and D_{Si} were obtained from [9]. The evolution of a precipitate p is limited by the constituent with the lowest concentration diffusing to the particle, i.e. the growth of Fe$_2$SiTi is limited by Ti, as there are less atoms available to form the intermetallic phase.

Results from classical nucleation theory provide the critical nucleation radius r_p^*, free energy of nucleation, ΔG_p^*, and nucleation rate, J_p, necessary to form a precipitate from a supersaturated solid solution [32]:

$$
\begin{aligned}
r_p^* &= -\frac{2\gamma_{int}}{\Delta G_v} \\
\Delta G_p^* &= \frac{4\pi}{3}(r_p^*)^2 \gamma_{int} \\
J_p &= \frac{dN_p}{dt} = N_0 Z \beta^* \exp\left(-\frac{\Delta G_p^*}{k_B T}\right) \exp\left(-\frac{\tau}{t}\right),
\end{aligned} \tag{7}
$$

where γ_{int} is the matrix/precipitate interfacial energy, ΔG_v is the volumetric free energy, N_0 are the potential nucleation sites for precipitation, and $Z = \frac{V_m}{2\pi r_p^* N_a} \sqrt{\frac{\gamma_{int}}{k_B T}}$, $\beta^* = \frac{4\pi r_p^* D_p x_{\alpha'}}{a^4}$ and $\tau = \frac{2}{\pi \beta^* Z^2}$ are constants dictated by the particle's molar volume V_m, critical radius for nucleation, interfacial energy and concentration of the constituent in the matrix towards forming the precipitates, $x_{\alpha'}$. The number of initial nucleation sites available is assumed equal to the number of solute atoms per unit

16

volume: $N_0 = \frac{x_{Ti}}{a^3}$, where x_{Ti} is the nominal atom concentration of Ti in the alloy.

615 $\Delta G_v = \frac{\Delta G}{V_m}$ is computed using Thermocalc to obtain the Thermodynamic free energy, ΔG, of Fe$_2$SiTi in Fe-10Mn-1Si-1Ti with changing Ti concentration in the matrix and assuming that Si decreases accordingly.

Particle growth and coarsening are given by Zener's law [9]:

$$\frac{dr_p}{dt}\Big|_{growth} = \frac{D}{r_p}\frac{x_{\alpha'} - x_{int}}{x_p - x_{int}},$$

$$x_{int} = x_{int,eq}\exp\left(\frac{2\gamma_{int}V_m}{r_p R_g T}\right) \quad (8)$$

where R_g is the gas constant and x_{int} is the concentration at the matrix/particle

620 interface, given by the Gibbs–Thomson relation in the second equation, and $x_p = 0.25$ is the equilibrium concentration of Ti in Fe$_2$SiTi.

The particle volume fraction and effective concentration of Ti in the α' are given by:

$$f_p = 4N_p\frac{4\pi}{3}(r_p)^3$$

$$x_{\alpha'} = \frac{(x_{Ti} - 0.25f_p)}{(1 - f_p)} \quad (9)$$

where the 4 pre-factor in f_p accounts for the effective increment in the volume fraction

625 when the Ti diffuses to Fe$_2$SiTi, a multicomponent intermetallic [32]. The effective concentration of Ti in the matrix will dictate the evolution rate of the precipitates, as the content of each constituent in the matrix decreases until reaching an equilibrium concentration. N_p, r_p and f_p are obtained by solving simultaneously equations 7 and 8.

630 The transition from particle growth to coarsening is taken when the solution of equation 8 equals the LSW equation:

$$r_p|_{coars} = \left(r_0^3 + k_{LSW}t\right)^{1/3}, \quad (10)$$

where r_0 is the initial radius, taken as $\frac{a}{2}$, and k_{LSW} is a constant given by [29]:

$$k_{LSW} = \frac{8\gamma_{int}V_m D_p x_p}{9R_g T}. \quad (11)$$

Equation 10 operates after $r_p|_{coars} > r_p|_{growth}$ at a constant volume fraction, therefore after this point the particle number density changes according to $N_p = \frac{f_p}{\frac{4}{3}\pi(r_p|_{coars})^3}$.

635 *A.2 Austenite reversion modelling*

The thickness, r_γ, and length, L_γ, of austenite within a single lath has been prescribed by grain boundary kinetics equations [4]:

$$\frac{dr_\gamma}{dt} = M_{GB}\left(\frac{\Gamma_\gamma}{r_\gamma} - \frac{\Gamma_\gamma}{d_{lath}f_{\gamma,eq}^{1/3}}\right)$$

$$\frac{dL_\gamma}{dt} = M_{GB}\frac{2d_{block}}{d_{lath}}\left(\frac{\Gamma_\gamma}{L_\gamma} - \frac{\Gamma_\gamma}{d_{block}f_{\gamma,eq}^{1/3}}\right), \quad (12)$$

where Γ_γ is the α/γ interfacial energy, M_{GB} is the grain boundary mobility and $f_{\gamma,eq}$ is the equilibrium fraction of austenite. The mobility is dictated by grain boundary

17

640   diffusion: $M_{GB} = \frac{b_{\alpha'}^2}{k_B T} D_{\alpha',\gamma}$ where $D_{\alpha',\gamma} = \left(\frac{x_{Fe,\gamma}}{D_{Fe}} + \frac{x_{Mn,\gamma}}{D_{Mn}}\right)^{-1}$ is the effective diffu-
sion coefficient driving the $\alpha' \rightarrow \gamma$ transformation and $b_{\alpha'} = 0.286$ nm is the lattice
parameter of α'; $x_{Fe,\gamma}$ and $x_{Mn,\gamma}$ are the equilibrium concentrations of Fe and Mn
in γ, respectively, and D_{Fe} and D_{Mn} are the diffusion coefficients of Fe and Mn in
$\alpha'-$Fe, respectively. The interfacial energy was found to be strongly dependent upon
645   Mn concentration and it is given by [4]: $\Gamma_\gamma = 0.8 \exp(15 x_{Mn})$ J m^{-2}, where x_{Mn} is
the atom fraction of Mn in the steel.

     The volume fraction of γ is given by the ratio between the volume of transforming
austenite $(r_\gamma^2 L_\gamma)$ and the volume of an α' lath:

$$f_\gamma = \frac{r_\gamma^2 L_\gamma}{d_{lath}^2 d_{block}}. \tag{13}$$

This equation provides a direct link between the size of the reverted austenite and its
650   volume fraction without the need of additional parameters.

A.3 Calculations of peak hardness vs. ageing kinetics

     The simulations for Figure 10 were obtained by computing the time to reach 1HV
below the peak hardness using equations 2, 4 and 6-10. The results were then fitted to
functions in the form $A \ln(t) + B$ for simplicity in the analysis; to do this, simulations
655   for each steel in Table 2 were run for at least 3 different ageing temperatures. The only
input parameters for the precipitation models are the intermetallic interfacial energy
and molar volume, which were defined to match precipitation evolution of commercial
maraging steels tested in previous work [4]. The values of the interfacial energy used
for the simulations are 40 mJ m^{-2}, 50 mJ m^{-2} and 20 mJ m^{-2} for NiAl, Ni$_3$Ti and Cu
660   (bcc), respectively, whereas the molar volumes used are 10×10^{-6} m^3 mol^{-1}, 9×10^{-6}
m^3 mol^{-1} and 10×10^{-6} m^3 mol^{-1} for NiAl, Ni$_3$Ti and Cu (bcc), respectively.

Table 1: Cost comparison by Alloy addition (USD/wt.% per tonne), over that of hot rolled coil (Fe) using ferroalloy additions where appropriate, for a range of maraging steels [17].

	Fe	FeCr	FeNi	Co	Mo	FeTi	Al	FeMn	Cu	Ferro-Si			
\$ / wt% alloy / tonne	390	8060	7470	83250	18000	7220	2140	1960	6970	2170			
Reference	[33]	[34]	[35]	[36]	[33]	[34]	[36]	[34]	[36]	[34]			
	Fe	Cr	Ni	Co	Mo	Ti	Al	Mn	Cu	Si	Cost	M_s	$f_{retained}$
Alloy	(%)	(%)	(%)	(%)	(%)	(%)	(%)	(%)	(%)	(%)	(£/tonne)	(°C)	(%)
PH13-8Mo [1]	75.8	12.7	8.2		2.2		1.1				2350	316	4
C300 [18]	67.1		18.8	8.5	4.8	0.8	0.1				9660	222	11
M350 [19]	74.8		18.9	0.2	4.1	1.9	0.1				2760	153	24
LeanLAl [6]	86.8		2.0		1.0	1.0	0.2	9.1			920	274	6.4
1RK91 [37]	73.1	12.2	9.0		4.0	0.9	0.3	0.3	2.0	0.2	2740	283	5.8
PH17-4 [38]	79.3	16.2	3.9					0.5	3.4		1920	244	9
Fe-10Mn-1Si-1Ti	88.0					1.0		10.0		1.0	633	273	6.5

19

Table 2: Comparison of precipitate types and volume fraction.

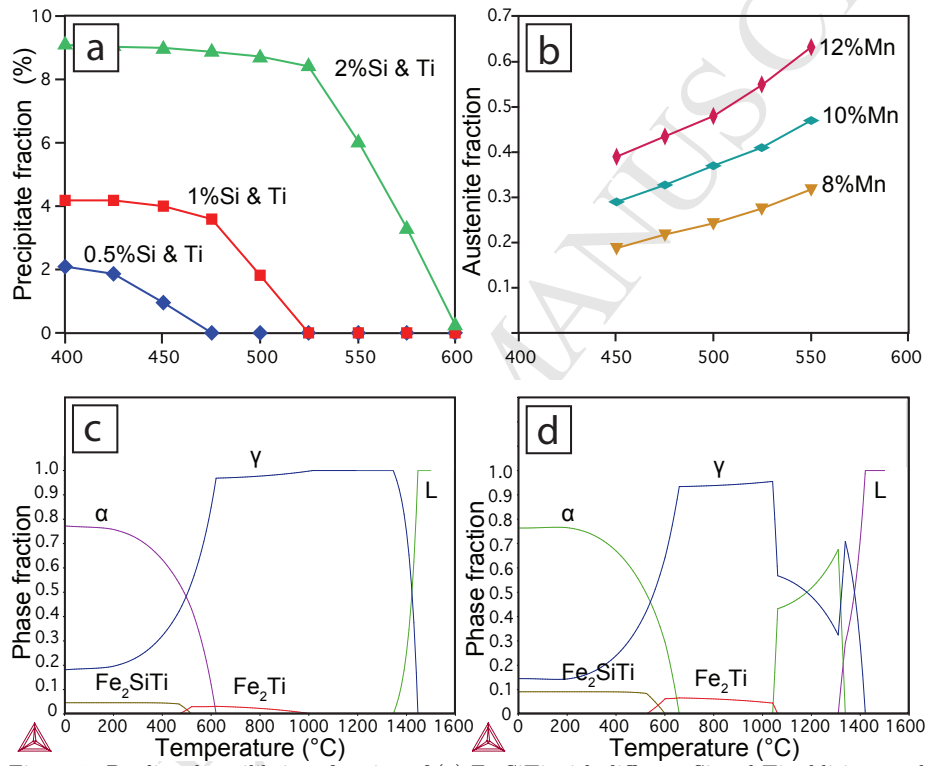| Steel	Precipitate	Volume fraction (%)
Fe-10Mn-1Si-1Ti	Fe_2SiTi	4.2
Fe-10Mn-2Ni-1Al	NiAl	4.1
Fe-17.5Ni-1Ti	Ni_3Ti	4
Fe-10Mn-5Cu	Cu (bcc)	3.5

Figure 1: Predicted equilibrium fraction of (a) Fe$_2$SiTi with different Si and Ti additions and (b) austenite when varying Mn content. Equilibrium phase fractions for (c) Fe-10Mn-1Si-1Ti and (d) Fe-10Mn-2Si-2Ti.
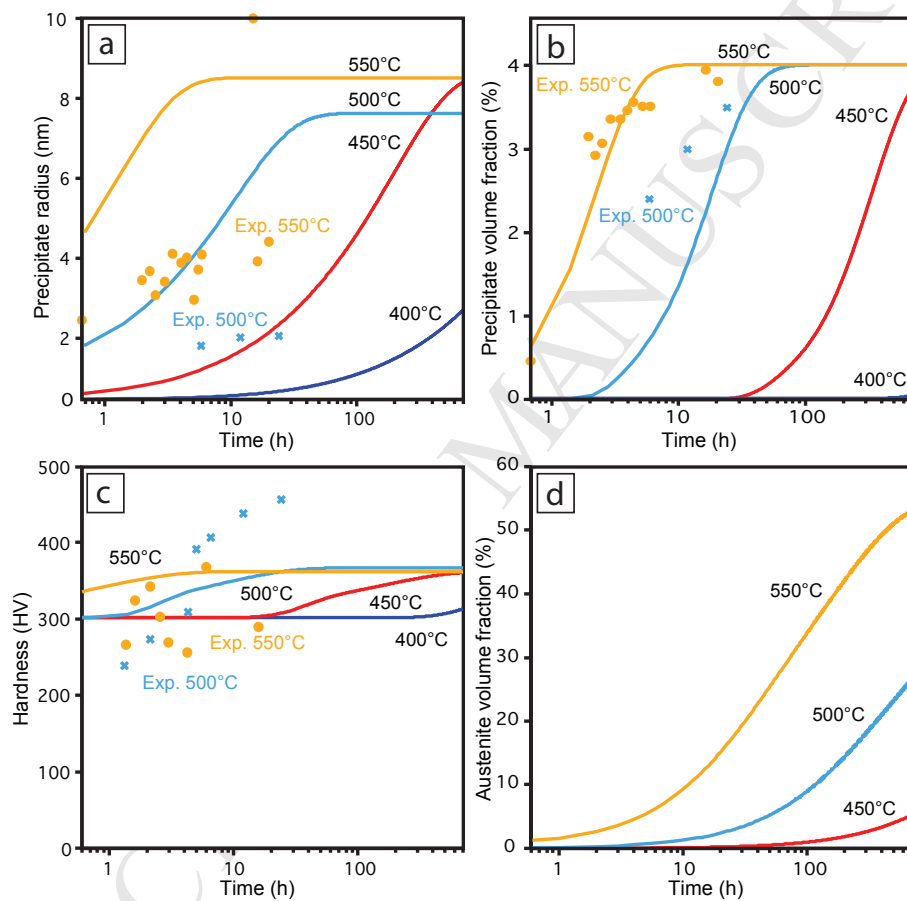
21

Figure 2: Predicted Fe$_2$SiTi (a) radius and (b) volume fraction, and (c) resulting Hardness. (d) Predicted reverted austenite fraction. Experimental data obtained from [9].

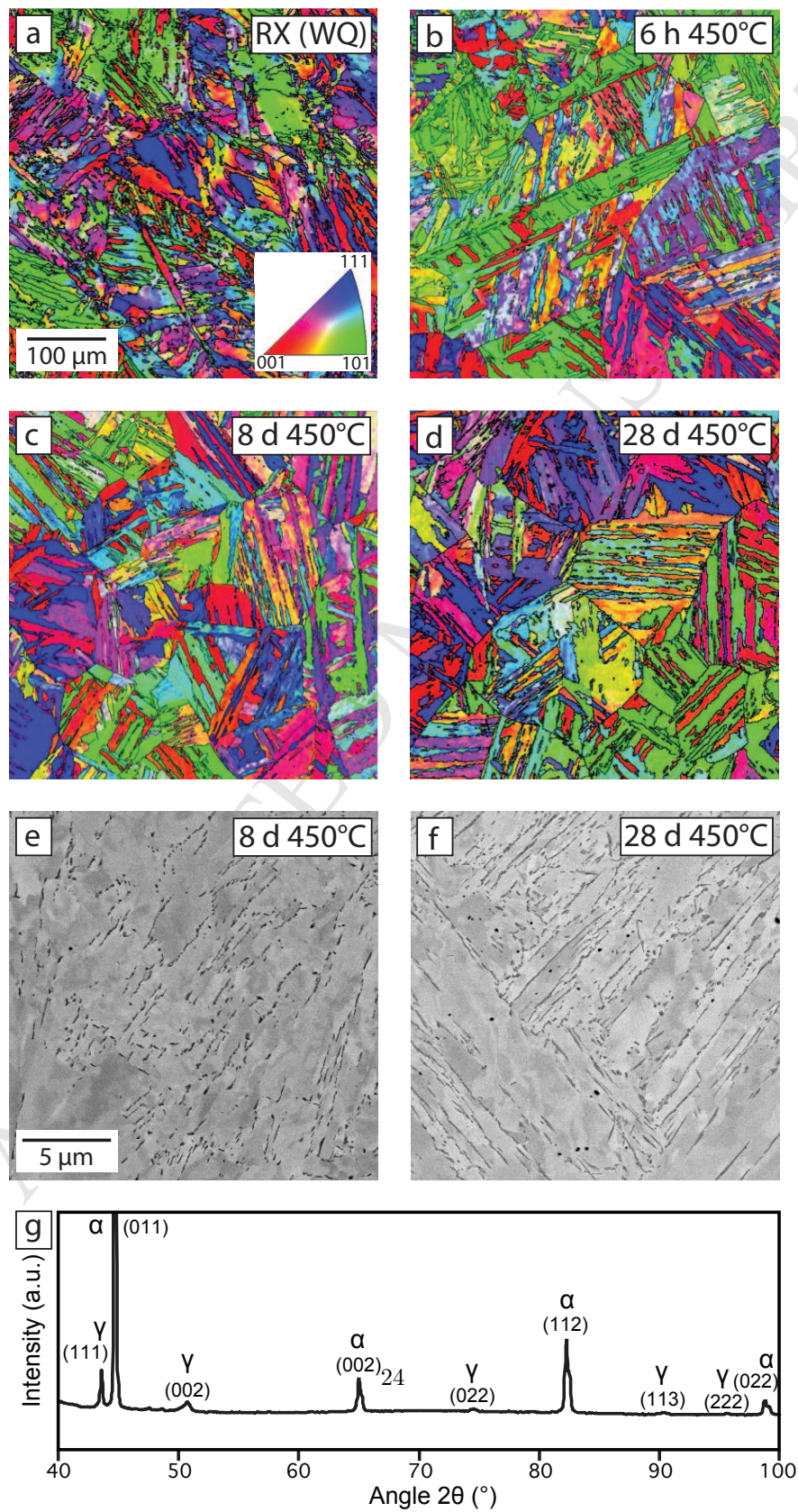22
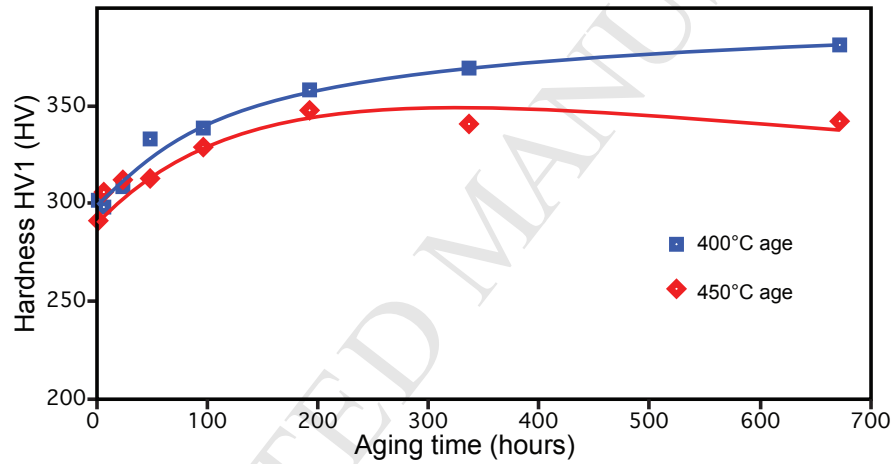
Figure 3: Fe-Mn-Si-Ti steel age hardening curves at $400\,^{\circ}\mathrm{C}$ (blue) and $450\,^{\circ}\mathrm{C}$ (red).

Figure 4: Fe-Mn-Si-Ti steel SEM EBSD IPF-Z maps in (a) following recrystalision at 1200 °C
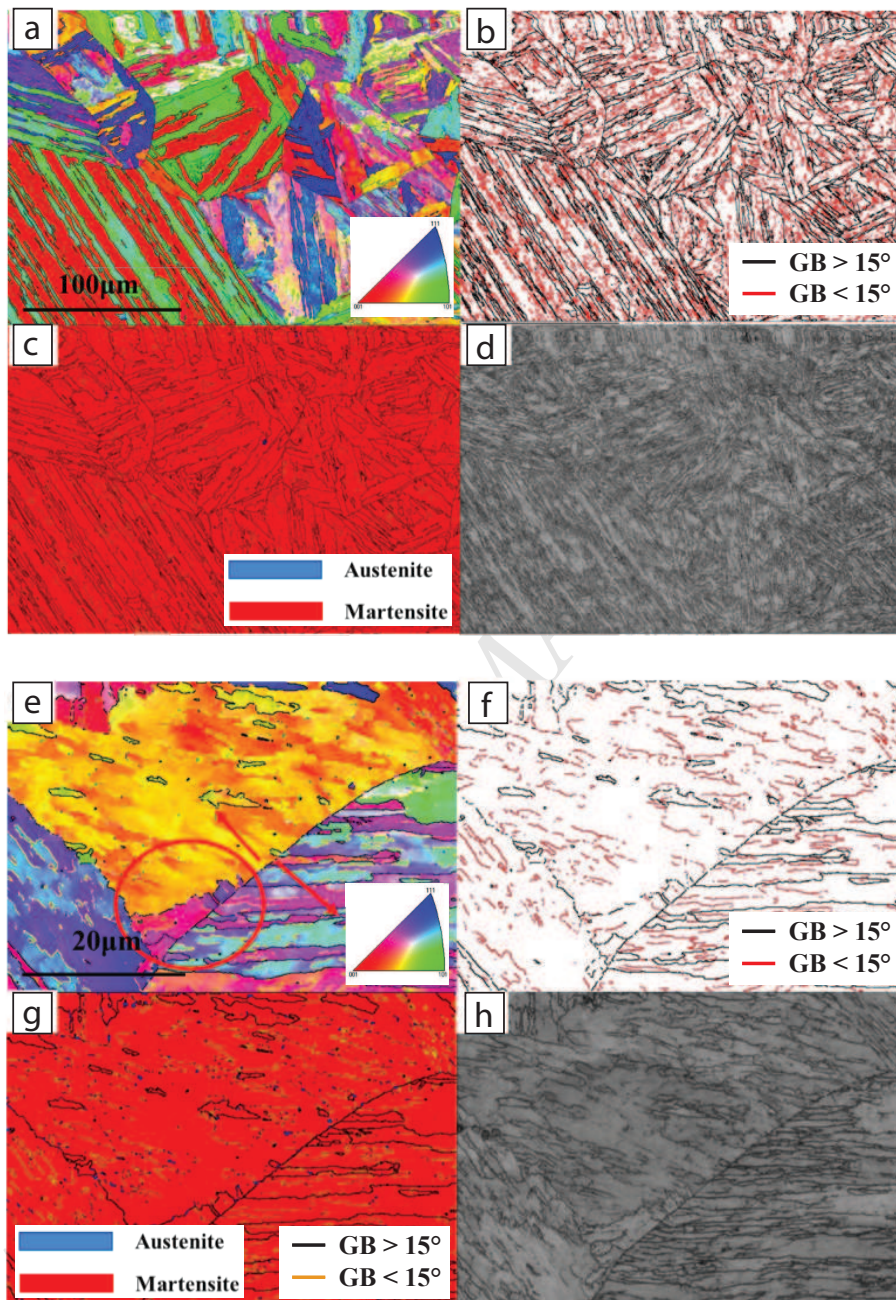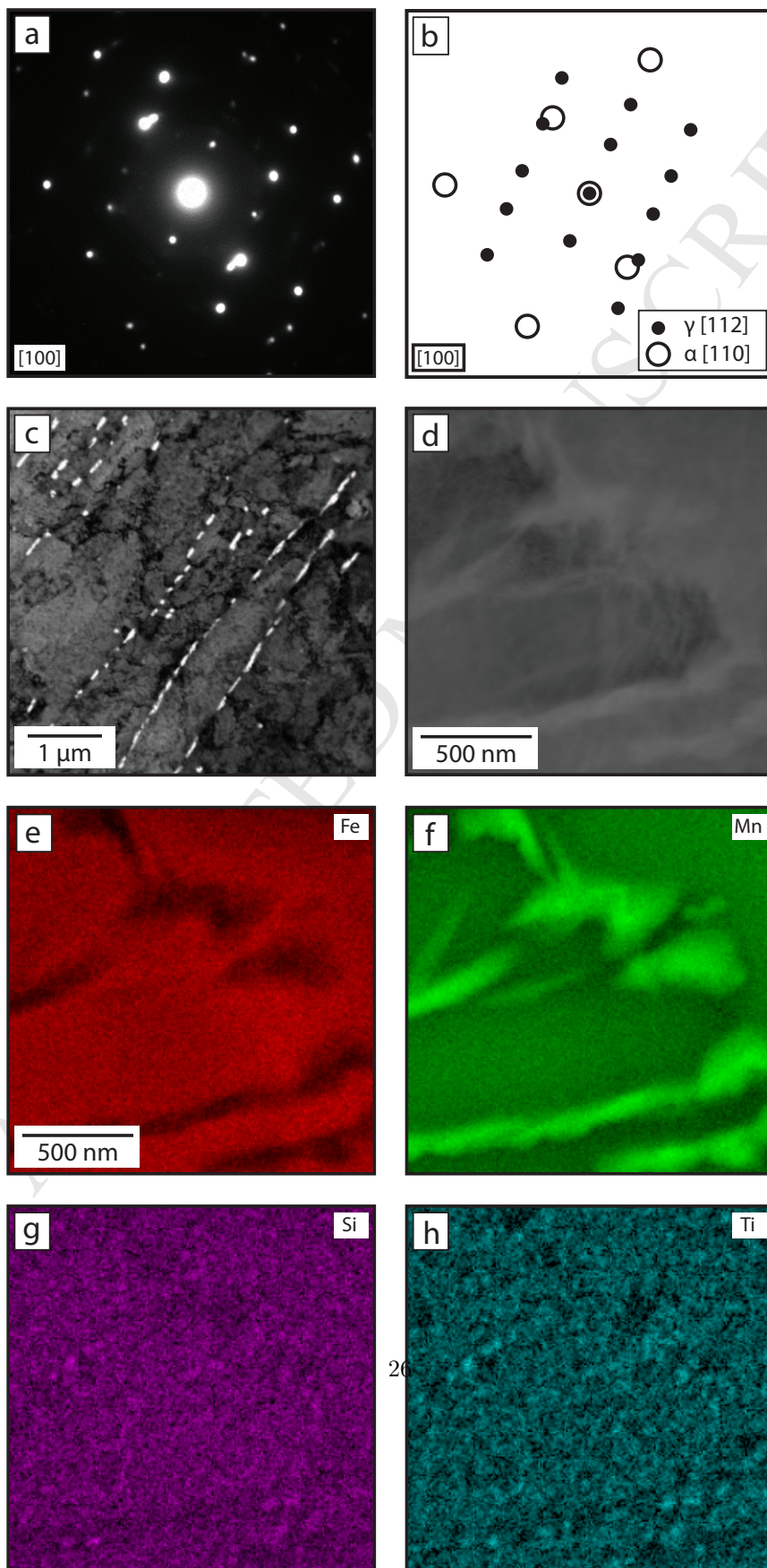
Figure 5: 450 °C for 4 weeks aged alloy EBSD derived maps of (a) IPF-Z, (b) grain boundaries, (c) phases and (d) band contrast map, as well as detailed maps (e) IPF-Z, (f) grain boundaries, (g) phases and (h) band contrast.
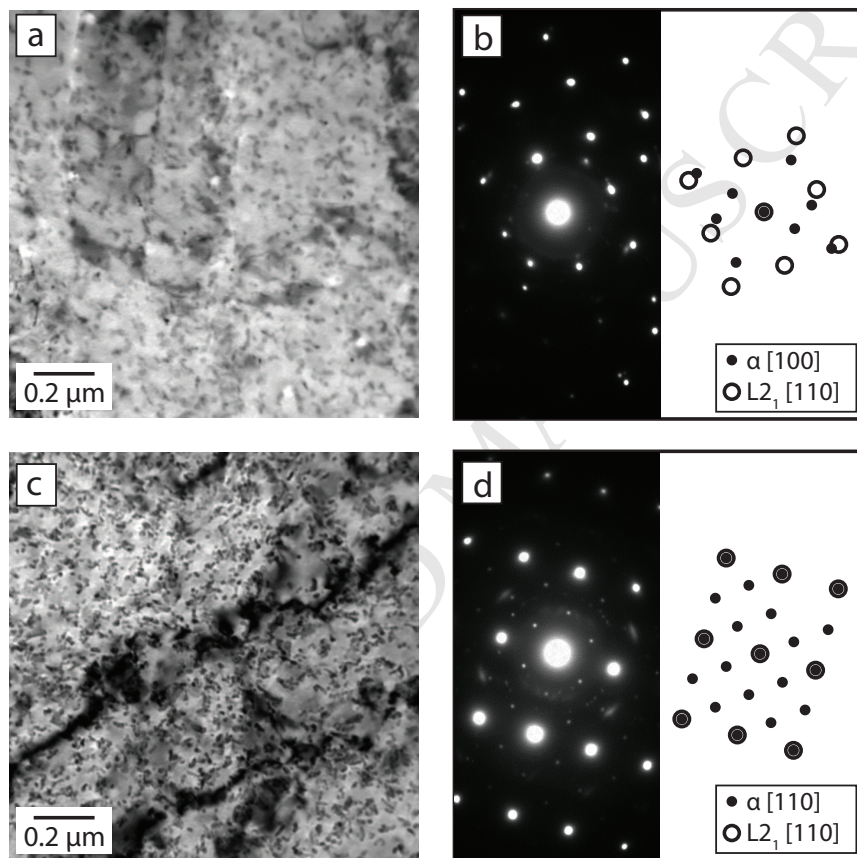
26

Figure 7: TEM on an electropolished foil of the alloy aged at 450 °C for 8 days, (a) bright field image, (b) SADP with corresponding key, (c) bright field image, (d) SADP with corresponding key.
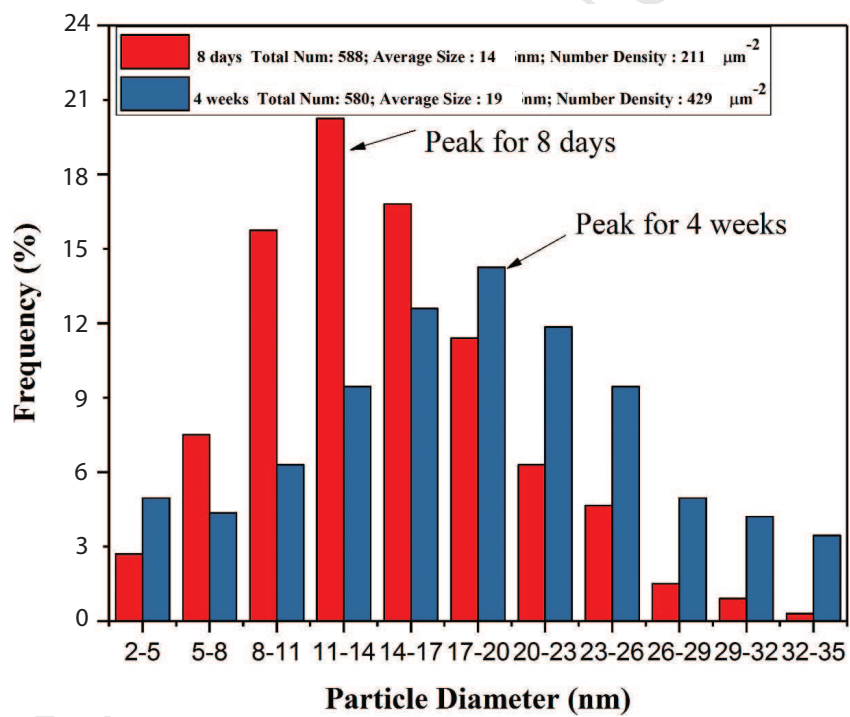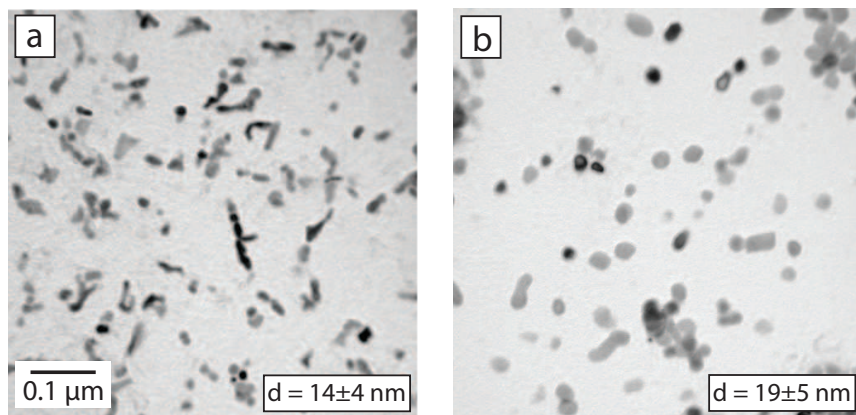
27

Figure 8: TEM on an carbon replica of, (a) extracted particles from the alloy aged at 450 °C for 8 days, (b) extracted particles from the alloy aged at 450 °C for 4 weeks, c) Particle size distribution
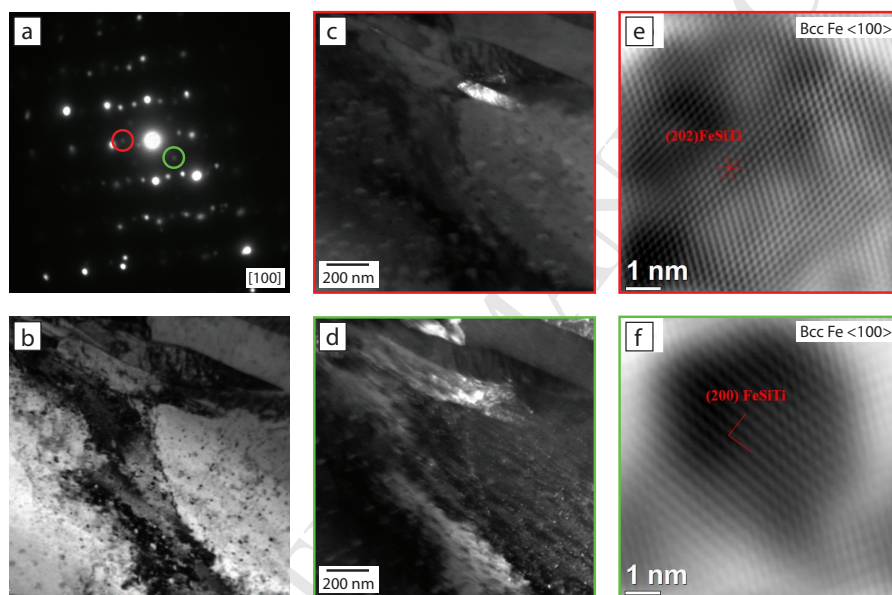
Figure 9: TEM following aging at 450 °C for 4 weeks FIB sample (a) SADP, (b) bright field image, (c) dark field image produced using the red circled reflection, (d) dark field image produced using the green circled reflection. HR-TEM, in the 450 °C, 8 d electropolished sample, of (e) a larger ~ 15 nm L2$_1$ Fe$_2$SiTi precipitate, and (f) a smaller ~ 5 nm precipitate.
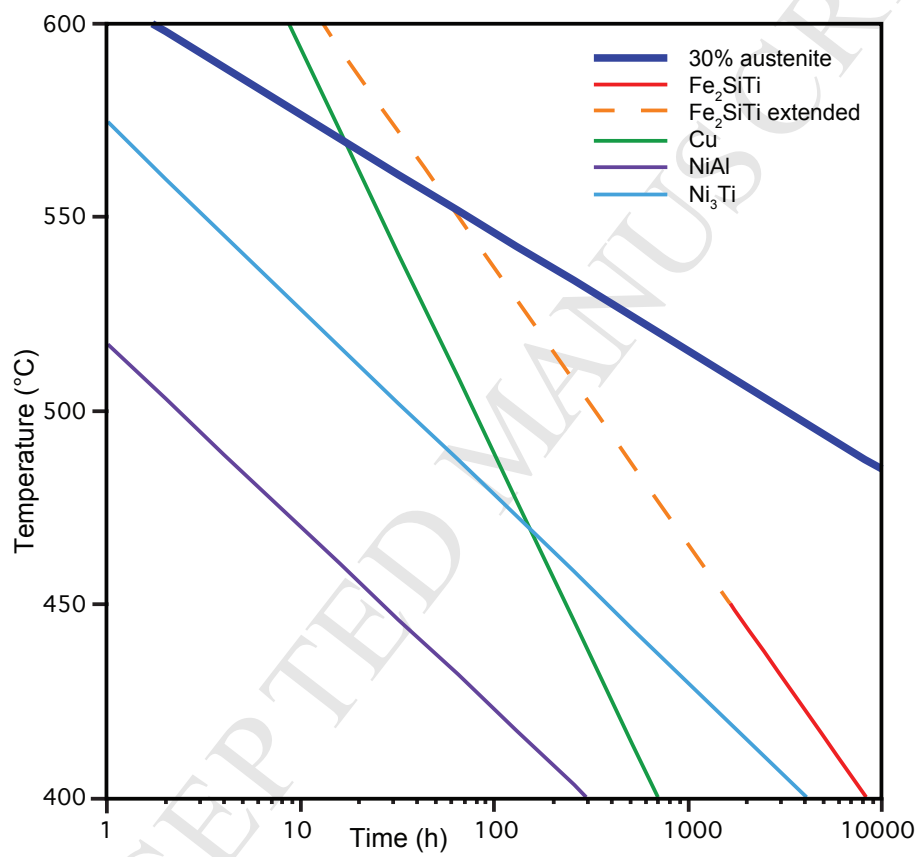
Figure 10: Comparison of ageing kinetics of a number of intermetallic precipitates within maraging steels

a — Precipitate radius (nm) vs Time (h): 550°C, 500°C, 450°C, 400°C; Exp. 550°C, Exp. 500°C

b — Precipitate volume fraction (%) vs Time (h): 550°C, 500°C, 450°C, 400°C; Exp. 550°C, Exp. 500°C

c — Hardness (HV) vs Time (h): 550°C, 500°C, 450°C, 400°C; Exp. 550°C, Exp. 500°C

d — Austenite volume fraction (%) vs Time (h): 550°C, 500°C, 450°C

a

b

• α [100]
○ L2₁ [110]

c

0.2 µm

d

• α [110]
○ L2₁ [110]

a [100]

c 200 nm

e Bcc Fe <100>
(202)FeSiTi
1 nm

b

d 200 nm

f Bcc Fe <100>
(200) FeSiTi
1 nm